Inorganic Chemistry

Article

pubs.acs.org/IC

Probing $Ni[S_2PR_2]_2$ Electronic Structure to Generate Insight Relevant to Minor Actinide Extraction Chemistry

Scott R. Daly, Jason M. Keith, Enrique R. Batista,* Kevin S. Boland, Stosh A. Kozimor,* Richard L. Martin, and Brian L. Scott

Los Alamos National Laboratory, Los Alamos, New Mexico 87545, United States

Supporting Information

ABSTRACT: A method to evaluate the electronic structure of minor actinide extractants is described. A series of compounds containing effective and ineffective actinide extractants (dithiophosphinates, $S_2PR_2^-$) bound to a common transition metal ion (Ni^{2+}) was analyzed by structural, spectroscopic, and theoretical methods. By using a single transition metal that provides structurally similar compounds, the metal contributions to bonding are essentially held constant so that subtle electronic variations associated with the extracting ligand can be probed using UV-vis spectroscopy. By comparison, it is difficult to obtain similar information using analogous techniques with minor actinide and lanthanide complexes. Here, we demonstrate that this approach, supplemented with ground state and time-dependent density functional theory, provides insight for understanding why high separation factors are reported for the extractant $HS_2P(o\text{-}CF_3C_6H_4)_2$, while lower values are reported and anticipated for other HS_2PR_2 derivatives (R = C_6H_5, $p\text{-}CF_3C_6H_4$, $m\text{-}CF_3C_6H_4$). The implications of these results for correlating electronic structure with the selectivity of HS_2PR_2 extractants are discussed.

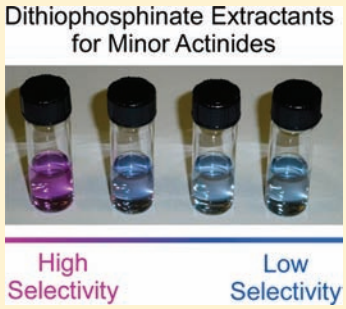

INTRODUCTION

Proposed advanced nuclear fuel cycles offer a means to responsibly manage inventories of spent nuclear fuel and an opportunity to meet increasing global energy demands without relying on carbon-based energy sources.[1−5] One of the greatest chemical challenges facing the development of this technology involves removing the trivalent minor actinides (americium and curium) from lanthanide contaminants found in spent nuclear fuel.[6−8] Separating these elements is difficult because they have similar chemical and physical properties, including comparable ionic radii, a common +3 oxidation state, and redox chemistry that is difficult to access.[9] In the course of developing improved minor actinide/lanthanide separation methods,[6−8,10−16] it has been established that minor actinides can be effectively removed from lanthanides through liquid/liquid extraction using certain "soft-donor" extractants, particularly those containing S or N.[17−29] Despite these empirical observations, it is not clear what factors contribute to soft-donor extraction selectivity.

It has long been suggested that the separation of minor actinides from lanthanides can be heavily influenced by special attributes associated with the electronic structure of the extracting ligand, which is proposed to lead to more covalent metal−ligand bonding with actinide vs lanthanide elements.[9,30,31] While only subtle differences in metal−ligand covalency between trivalent minor actinides and lanthanides are expected,[32,33] such differences could be large enough to account for the observed selectivity in soft-donor separations.[34−36] However, at present, it is difficult to determine what electronic properties influence the binding selectivity of an extractant in *f*-element separations.

Here, we describe the latest in a series of studies[36−38] focused on understanding how extractant electronic structure affects binding selectivity in minor actinide separations. Although new coordination compounds are reported, this manuscript focuses on evaluating a series of effective and ineffective extractants bound to a common metal ion so that the metal contributions to the bonding are held constant and only electronic variations associated with the ligand orbitals are probed. Described are the syntheses, molecular structures, spectroscopy, and density functional theory (DFT) calculations for a family of complexes that contain diaryldithiophosphinate ligands. The $S_2PR_2^-$ ligands, where R = $o\text{-}CF_3C_6H_4$, $m\text{-}CF_3C_6H_4$, $p\text{-}CF_3C_6H_4$, and C_6H_5 (Ph), were chosen because their selectivity for minor actinides varies dramatically with the presence and position of the CF_3 substituent. For example, the *ortho*-substituted $HS_2P(o\text{-}CF_3C_6H_4)_2$ provides exceptionally high separation factors (SF) for americium over europium (SF = 100 000).[39] The selectivity drops to 1000 for the *meta*-substituted $HS_2P(m\text{-}CF_3C_6H_4)_2$,[40] and based on previous reports, the SFs for $HS_2P(p\text{-}CF_3C_6H_4)_2$ and HS_2PPh_2 are anticipated to be even lower.[24] Binding these extractants to Ni^{2+} results in structurally similar and highly symmetric $Ni[S_2PR_2]_2$ complexes with relatively well understood electronic structures. The divalent nickel ion is additionally attractive because it provides a well-established platform for identifying electronic nuances associated with the ligand as they pertain to metal−ligand bonding *via* UV−vis spectroscopy.[41−48] By comparison, it is difficult to obtain equivalent information from analogous UV−

Received: January 20, 2012
Published: June 29, 2012

Table 1. Crystallographic Data for $Ni[S_2PR_2]_2$ Complexes (R = *o*-$CF_3C_6H_4$, 1; *m*-$CF_3C_6H_4$, 2; *p*-$CF_3C_6H_4$, 3; Ph, 4) Collected at 120(1) K

	1	2	3	4	4[a]
formula	$C_{28}H_{16}F_{12}NiP_2S_4$	$C_{28}H_{16}F_{12}NiP_2S_4$	$C_{28}H_{16}F_{12}NiP_2S_4$	$C_{24}H_{20}NiP_2S_4$	$C_{24}H_{20}NiP_2S_4$
FW (g mol^{-1})	829.30	829.30	829.30	557.29	557.29
cryst syst	monoclinic	monoclinic	monoclinic	monoclinic	monoclinic
space group	$P2_1/c$	$P2_1/c$	$P2_1/c$	$P2_1/n$	$C2/c$
a (Å)	9.179(3)	12.032(2)	10.803(6)	13.033(2)	13.28(1)
b (Å)	7.876(3)	9.978(2)	11.195(6)	11.442(2)	11.55(1)
c (Å)	20.948(7)	12.864(2)	13.291(7)	16.641(2)	17.00(1)
β (deg)	95.952(4)	92.663(2)	92.802(6)	103.362(1)	103.43(5)
V ($Å^3$)	1506.1(8)	1542.7(5)	1606(2)	2414(5)	2533
Z	2	2	2	4	4
ρ_{calcd} (g cm^{-3})	1.829	1.785	1.715	1.533	1.461
μ (mm^{-1})	1.124	1.098	1.055	1.293	0.0525
data/restraints/params	4146/0/215	2820/0/214	3065/48/242	5742/0/283	864
goodness-of-fit on F^2	1.138	1.059	1.141	1.135	
R_1 [$I > 2\sigma(I)$][b]	0.0515	0.0423	0.0416	0.0397	0.114
wR_2 (all data)[c]	0.1718	0.1042	0.1005	0.1460	
largest diff. peak and hole (e·$Å^{-3}$)	0.804/−0.487	0.723/−0.562	0.861/−0.678	0.522/−0.619	

[a]Obtained from ref 42. Data collected at room temperature using Cu Kα radiation. [b]$R_1 = \sum ||F_o| - |F_c||/|\sum|F_o|$ for reflections with $F_o^2 > 2\sigma(F_o^2)$. [c]$wR_2 = [\sum w(F_o^2 - F_c^2)^2/\sum(F_o^2)^2]^{1/2}$ for all reflections.

Table 2. Selected Bond Distances and Angles for $Ni[S_2PR_2]_2$ Complexes[a]

$Ni[S_2PR_2]_2$	Ni−S (Å)	S−P (Å)	P−C (Å)	S−Ni−S (deg)	S−P−S (deg)	C−P−C (deg)	S−P−C (deg)
$Ni[S_2P(o\text{-}CF_3C_6H_4)_2]_2$ (1)	2.215(1)	2.016(2)	1.825(5)	87.86(4)	99.55(7)	107.2(2)	112.1(2)
	2.220(1)	2.014(2)	1.827(5)				112.0(2)
	[2.218]	[2.015]	[1.826]				112.6(2)
							113.5(2)
$Ni[S_2P(m\text{-}CF_3C_6H_4)_2]_2$ (2)	2.2343(9)	2.005(1)	1.804(4)	88.48(3)	102.15(6)	104.6(2)	112.0(1)
	2.2431(9)	2.010(1)	1.805(4)				112.5(1)
	[2.239]	[2.008]	[1.804]				112.7(1)
							113.1(1)
$Ni[S_2P(p\text{-}CF_3C_6H_4)_2]_2$ (3)	2.232(1)	2.007(2)	1.803(4)	88.79(4)	102.13(6)	106.6(2)	110.8(1)
	2.239(1)	2.015(2)	1.807(4)				110.1(1)
	[2.236]	[2.011]	[1.805]				113.7(1)
							113.7(1)
$Ni[S_2PPh_2]_2$ (4)	2.2161(7)	2.016(1)	1.797(3)	88.47(3)	100.66(4)	107.5(1)	111.7(1)
	2.2342(7)	2.017(1)	1.807(3)				112.6(1)
	[2.225]	[2.017]	[1.802]				112.6(1)
							111.8(1)
$Ni[S_2PPh_2]_2$ (4)[b]	2.234(5)	2.006(8)	1.79(2)	88.2(1)	101.2(2)	107.1(6)	112.2(4)
	2.242(6)	2.022(8)	1.78(2)				112.1(5)
	[2.238]	[2.014]	[1.78]				111.2(4)
							112.3(5)

[a]Average bond distances are shown in brackets. [b]Obtained from ref 42.

vis experiments on *f*-element dithiophosphinate complexes due to lower symmetry and smaller ligand field effects.[49] The experimental and theoretical results are discussed in relation to recent S K-edge X-ray absorption spectroscopy (XAS) and time-dependent density functional theory (TDDFT) calculations conducted on the free $S_2PR_2^-$ ligands,[38] which suggest that the electronic structure of the $S_2PR_2^-$ extractant can be correlated with its minor actinide selectivity.

RESULTS AND DISCUSSION

Synthesis and Characterization of $Ni[S_2PR_2]$ Complexes. The $Ni[S_2PR_2]_2$ complexes, where R = *o*-$CF_3C_6H_4$ (1), *m*-$CF_3C_6H_4$ (2), and *p*-$CF_3C_6H_4$ (3) were prepared in air by treating $NiCl_2·6H_2O$ with two equivalents of HS_2PR_2 in water and EtOH (eq 1).

$$NiCl_2 + 2HS_2PR_2 \rightarrow Ni[S_2PR_2]_2 + 2HCl \quad (1)$$

The CF_3-free $Ni[S_2PPh_2]_2$ (4), which has been reported previously,[42,45] was also prepared for spectroscopic and structural comparison to 1−3. All four compounds precipitate from the reaction solutions as they are formed, but there are noticeable differences in how the reactions proceed. For example, while the addition of $HS_2P(o\text{-}CF_3C_6H_4)_2$ to a solution of $NiCl_2$ causes 1 to immediately precipitate, the synthesis of 2 and 3 required heating and longer reaction times. In the course of exploring these differences, an alternative procedure was developed that appears to expedite the synthesis of 2 and 3.

dx.doi.org/10.1021/ic3001587 | Inorg. Chem. 2012, 51, 7551−7560

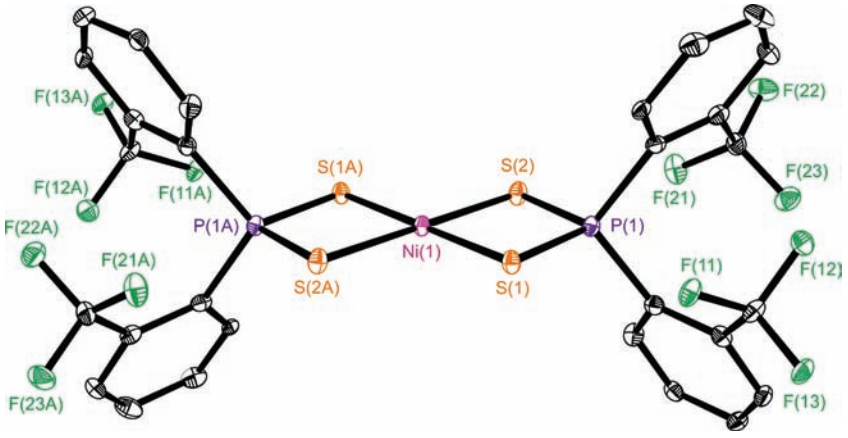

Figure 1. Molecular structure of $Ni[S_2P(o\text{-}CF_3C_6H_4)_2]_2$, **1**. Ellipsoids are drawn at the 35% probability level. The hydrogen atoms were included in the refinement but have been omitted from the figure.

This approach utilizes biphasic reaction conditions achieved by contacting concentrated aqueous solutions of $NiCl_2$ and HS_2PR_2 mixtures with CH_2Cl_2. While it is not immediately clear to us why this approach proceeds more rapidly than the precipitation route, this approach provides a more efficient method for isolating **2** and **3** in moderate yields.

Single crystals suitable for X-ray diffraction studies were prepared by cooling concentrated CH_2Cl_2 solutions of **1**–**3** (Table 1). Crystals of $Ni[S_2PPh_2]_2$ (**4**) were also grown following the literature procedure (Figure S1, Supporting Information). However, in our hands, **4** crystallizes in the $P2_1/n$ space group, and not C_2/c as previously reported.[42] Despite the difference in space groups, only small variations are observed when the metrical parameters from both data sets are compared (Tables 1 and 2). Although *ortho*-substituted **1** forms magenta-colored crystals, its structure is remarkably similar to **2**–**4**, which crystallize as dark blue prisms. In each structure, the four sulfur atoms form a square-planar arrangement around the Ni^{2+} ion (Figures 1–3). The bond distances and angles for **1** are slightly different compared to those in **2** and **3**, which have identical metrics when their standard deviations are considered (Table 2). For example, the Ni–S bond distances for **1** are only 0.02 Å shorter and the P–C bond distances are only 0.02 Å longer compared to those in **2** and **3**. The S–P–S angles in *ortho*-substituted **1** at 99.55(7)° are comparable to those observed in $Ni[S_2PPh_2]_2$ (**4**) at 100.66(7)° but are subtly different compared to the S–P–S angles in *meta*- and *para*-substituted **2** and **3** at 102.15(6)° and 102.13(6)°, respectively. The most pronounced structural difference associated with **1**–**3** involves the planarity of the PS_2–Ni atoms. For **1**, this four-membered metallocycle is planar, but for **2** and **3** the phosphorus atom is puckered out of the NiS_4 plane by 0.18 Å and 0.39 Å, respectively. Analogous puckering is common in the solid-state structures of many diaryldithiophosphinates and has been attributed to intermolecular π–π van der Waals interactions.[50] Consistent with this analysis, inspection of the extended crystal structures shows no obvious intermolecular interactions for **1** but does reveal a possibility for intermolecular aryl π–π stacking interactions for **2** and **3** (Figure S2, Supporting Information). The observed π–π overlap in the structures of **2** and **3** appears to be accommodated by free rotation of the aryl groups around the P–C bond. By comparison, rotation of the aryl groups in **1** is likely obstructed by steric repulsion of the *o*-CF_3 substituents, which are locked between the S atoms and the CF_3 substituents on the adjacent aryl group. These steric interactions have been reported previously in the calculated and experimental structures of $S_2P(o\text{-}CF_3C_6H_4)_2^-$ and $HS_2P(o\text{-}CF_3C_6H_4)_2$.[37,39,51–53]

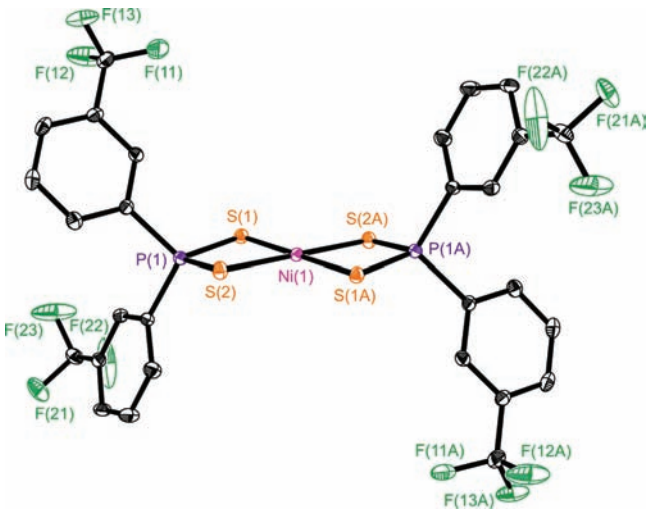

Figure 2. Molecular structure of $Ni[S_2P(m\text{-}CF_3C_6H_4)_2]_2$, **2**. Ellipsoids are drawn at the 35% probability level. The hydrogen atoms were included in the refinement but have been omitted from the figure.

In addition to unique reaction chemistry and slight structural differences, $Ni[S_2P(o\text{-}CF_3C_6H_4)_2]_2$ (**1**) also exhibits distinct NMR spectra. Single resonances observed in the decoupled ^{31}P and ^{19}F NMR spectra of *ortho*-substituted **1** are shifted dramatically to lower field compared to **2** and **3**. For instance, the ^{31}P NMR resonance for **1** is more deshielded at δ 92.3 compared to δ 80.2 and 79.6 for **2** and **3**, and the ^{19}F NMR resonance is similarly shifted at δ −57.6 compared to δ −64.1 (**2**) and −64.6 (**3**). The ^1H NMR spectra of **1**–**3** are readily assignable based on their peak integrations and isotopic splitting, and the observed trends in NMR chemical shifts are consistent with the trends previously reported for their corresponding HS_2PR_2 and $[PPh_4][S_2PR_2]$ compounds.[37]

In comparison to the NMR spectral, structural, and reactivity differences for **1** compared to **2** and **3**, the most profound distinction for **1** is associated with its magenta color. The unique color indicates that the electronic structure of **1** appreciably differs from the dark blue **2**–**4**. We have evaluated these differences using UV–vis spectroscopy, and the spectra of

dx.doi.org/10.1021/ic3001587 | Inorg. Chem. 2012, 51, 7551–7560

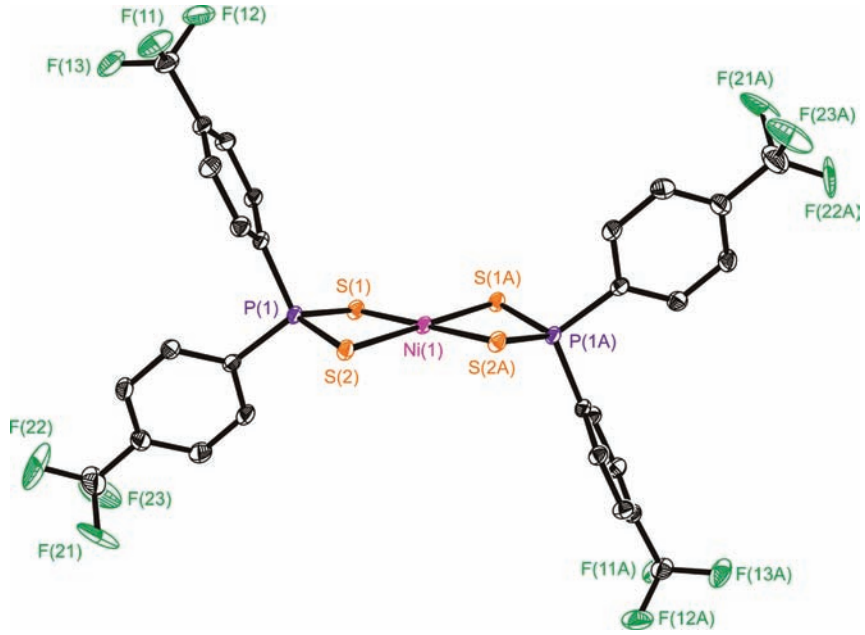

Figure 3. Molecular structure of $Ni[S_2P(p\text{-}CF_3C_6H_4)_2]_2$, **3**. Ellipsoids are drawn at the 35% probability level. The hydrogen atoms were included in the refinement but have been omitted from the figure.

1−**4** are provided in Figure 4. The profile of each spectrum is similar to those reported previously for square-planar Ni^{2+} dithiophosphinates.[43−48] A large charge transfer band is observed around 30 000 cm^{-1} and is adjacent to a lower energy shoulder at ca. 25 000 cm^{-1} in the UV region. In the visible region, there are two weak intensity features located between 12 500 and 23 000 cm^{-1} that have been assigned to dipole-forbidden d−d transitions (see below). The UV−vis spectra of $Ni[S_2P(m\text{-}CF_3C_6H_4)_2]_2$ (**2**) and $Ni[S_2P(p\text{-}CF_3C_6H_4)_2]_2$ (**3**), which are superimposable, are almost identical to the spectrum of $Ni[S_2PPh_2]_2$ (**4**), which does not have any electron withdrawing CF_3 substituents. In contrast, all of the UV−vis features for *ortho*-substituted **1** are shifted significantly to higher energies despite the structural similarities of **1**−**4** (Table 3). For example, the charge transfer band at

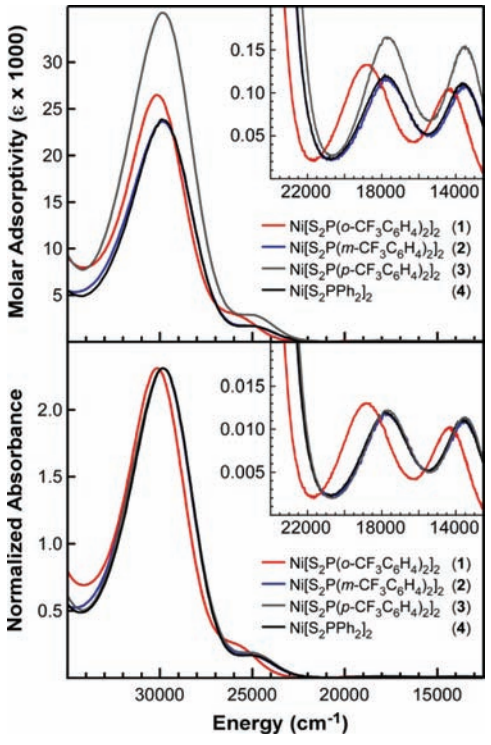

Figure 4. Top: UV−vis spectra for $Ni[S_2PR_2]_2$ (R = *o*-$CF_3C_6H_4$, **1**; *m*-$CF_3C_6H_4$, **2**; *p*-$CF_3C_6H_4$, **3**; Ph, **4**). The inset shows the magnified d−d transitions in the 24 000−12 500 cm^{-1} visible region. Bottom: Normalized UV−vis spectra to show the shifted features of **1** relative to **2**−**4**.

Table 3. Experimental UV−Vis Transitions for $Ni[S_2PR_2]_2$ Complexes 1−4. The Position of the Band Maxima are Reported in Units of 1000 cm^{-1}

1	**energy**	14.3	18.8	25.5	30.2
R = *o*-$CF_3C_6H_4$	**ε** (M^{-1} cm^{-1})	111	143	2120	26 900
2	**energy**	13.5	17.7	24.6	29.8
R = *m*-$CF_3C_6H_4$	**ε** (M^{-1} cm^{-1})	89	96	1590	23 300
3	**energy**	13.5	17.7	24.6	29.8
R = *p*-$CF_3C_6H_4$	**ε** (M^{-1} cm^{-1})	140	149	2650	34 100
4[a]	**energy**	13.6	17.8	24.9	29.8
R = phenyl	**ε** (M^{-1} cm^{-1})	96	101	1590	22 800

[a]Initially reported in ref 42 and verified here upon comparison.

30 200 cm^{-1} in **1** is blueshifted by more than 300 cm^{-1} while the two d−d transitions at 18 800 and 14 300 cm^{-1} are blueshifted by 800−1100 cm^{-1} compared to the identical features in **2**−**4**.

Ground-State Electronic Structure of $Ni[S_2PR_2]_2$. To facilitate interpretation of the UV−vis spectra shown in Figure 4, ground state density functional theory calculations (DFT) were made on compounds **1**−**4**. The optimized structures of **1**−**4** are consistent with the structures obtained from single-crystal XRD experiments, and the calculated bond distances, angles, and atomic coordinates can be found in the Supporting Information. In general, the molecular orbitals obtained from the DFT calculations are similar to those derived from a group theory analysis of $Ni[S_2PR_2]_2$. For example, for two generic

dx.doi.org/10.1021/ic3001587 | *Inorg. Chem.* 2012, 51, 7551−7560

$S_2PR_2^-$ ligands in D_{2h} symmetry there are S 3p symmetry adapted linear combinations (SALCs) of atomic orbitals of a_g and b_{1g} symmetries that can form Ni−S σ bonds using the Ni 3d orbitals of the same symmetry (d_{z^2} and d_{xy}). There are also S 3p SALCs of a_g, b_{2g}, and b_{3g} symmetry that are available to form Ni−S π bonds with the Ni $d_{x^2-y^2}$, d_{xz}, and d_{yz} orbitals (a_g, b_{2g}, and b_{3g}, respectively). A small energy difference is expected between the b_{2g} (d_{xz}) and the b_{3g} (d_{yz}) orbitals due to slight deviation of D_{2h}-Ni$[S_2PR_2]_2$ from D_{4h} symmetry. By comparison, in a perfectly symmetrical d^8 square-planar complex with monatomic ligands (D_{4h}-MX_4^{n-}), these two orbitals are degenerate. It should also be noted that lowering of the point group symmetry from D_{4h} to D_{2h} causes a change in the location of the $C_2(x)$ and $C_2(y)$ rotation axes, which coincide with the metal−ligand bonds in D_{4h}-MX_4^{n-} and lie between the Ni−S bonds in D_{2h}-Ni$[S_2PR_2]_2$.

The DFT calculations indicate that the lowest unoccupied molecular orbital (LUMO) has b_{1g} symmetry and is highest in energy due to the highly destabilized Ni−S σ^* bonds that result from strong directional overlap between Ni d_{xy} atomic orbital and the associated S b_{1g} SALC. The calculated energies for the remaining molecular orbitals decrease from d_{xy} (b_{1g}, LUMO) to d_{xz} (b_{2g}, HOMO), d_{yz} (b_{3g}), d_{z^2} (a_g), and $d_{x^2-y^2}$ (a_g). The quantitative molecular orbital diagram generated from the DFT calculations show that at lower energy are nonbonding and bonding molecular orbitals, which were not shown in the qualitative diagram provided in Figure 5. In this lower energy region, analysis of the Kohn−Sham orbitals shows that π-contributions from the ligand aryl groups cause additional splitting of the molecular orbitals containing Ni 3d character, particularly for those participating in Ni−S π-bonding ($d_{x^2-y^2}$, d_{xz}, and d_{yz}). This interpretation was confirmed by comparing the calculations on **1**−**4** with additional calculations conducted on Ni$[S_2PMe_2]_2$ (**5**), where analogous P−C(aryl) π-interactions are not present. Because the orbital splitting observed for Ni$[S_2PR_2]$ (R = *o*-$CF_3C_6H_4$, *m*-$CF_3C_6H_4$, *p*-$CF_3C_6H_4$, and Ph; **1**−**4**) is not present in the calculation for Ni$[S_2PMe_2]_2$, we conclude that the unique splitting in **1**−**4** is indeed associated with P−C π aryl interactions.

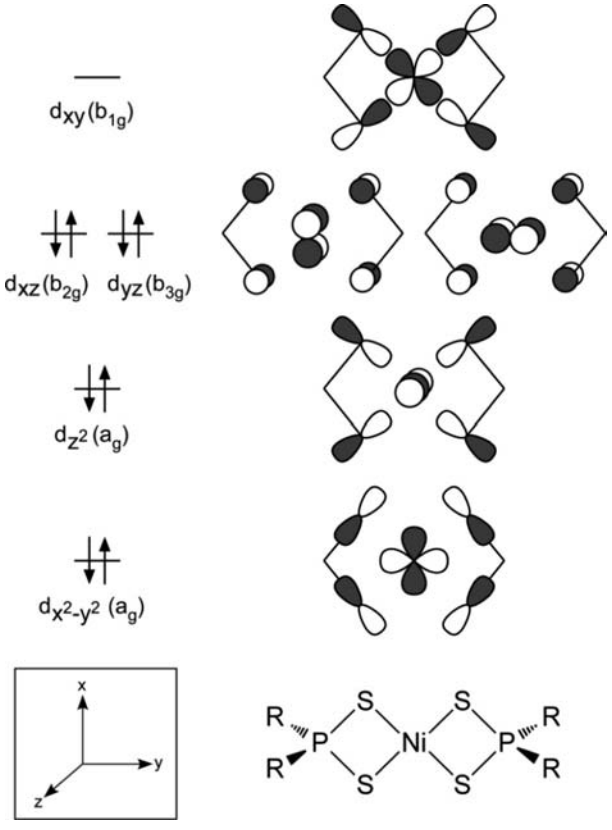

Figure 5. Qualitative ligand-field splitting diagram of Ni$[S_2PR_2]_2$ complexes in D_{2h} point group symmetry. Only the S 3p atomic orbitals are included from the $S_2PR_2^-$ ligands in the molecular orbitals to show the nature of the Ni−S bonds (σ^* vs π^*).

For the simplest complex in the series, Ni$[S_2PMe_2]_2$ (**5**), the calculations reveal that the MOs containing Ni d_{z^2} and $d_{x^2-y^2}$ character ($1a_g$ and $2a_g$; Figure 6) are essentially nonbonding

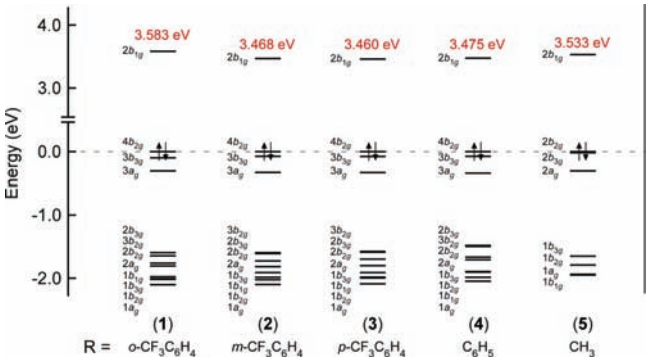

Figure 6. DFT calculated MO correlation diagram of Ni$[S_2PR_2]_2$ complexes **1**−**5**. The energies have been normalized so that the energy of the HOMO is 0.0 eV. The energies of the HOMO−LUMO gaps are shown in red.

with respect to sulfur, as evidenced by the lack of splitting into bonding and antibonding pairs and the low percentage of S 3p character (3.6%; Table 4). By comparison, the molecular orbitals containing Ni d_{xy}, d_{xz}, and d_{yz} character (b_{1g}, b_{2g}, and b_{3g}) all form bonding and antibonding pairs and have substantially more S 3p character (28.8−57.6%). The nonbonding nature of the Ni d_{z^2} and $d_{x^2-y^2}$ orbitals is consistent with calculations previously performed on the structurally similar D_{2h} Ni(II) dithiolenes.[54]

Overall, the calculated molecular orbital diagrams of **1**−**4** are remarkably similar, aside from one key difference: the HOMO−LUMO gap is nearly identical for **2**−**4** (3.460−3.475 eV) but increases by more than 0.1 eV (800 cm^{-1}) for *o*-CF_3 substituted **1** (3.583 eV). The magnitude of the increased HOMO−LUMO gap of **1** is consistent with its uniquely shifted UV−vis spectra, which is also shifted by 800−1100 cm^{-1} in comparison to **2**−**4**. While the origin of this shift is not immediately clear from the calculations reported here, it is consistent with our previous spectroscopic and theoretical analyses on $S_2PR_2^-$ ligands.[38] For example, S K-edge X-ray absorption spectroscopy (XAS) measurements and DFT calculations performed on the free anions show a large increase in S 3p mixing with the aryl π-orbitals for $S_2P(o\text{-}CF_3C_6H_4)_2^-$ relative to $S_2P(m\text{-}CF_3C_6H_4)_2^-$, $S_2P(p\text{-}CF_3C_6H_4)_2^-$, and $S_2PPh_2^-$. The increased mixing was accompanied by a concomitant increase of ~800 cm^{-1} in the calculated energy of the HOMO. It is important to point out that the HOMO for the $S_2P(o\text{-}CF_3C_6H_4)_2^-$ ligand is the same orbital involved in formation of the Ni−S σ bonds and appears to be associated with the uniquely shifted LUMO in Ni$[S_2P(o\text{-}CF_3C_6H_4)_2]_2$.

dx.doi.org/10.1021/ic3001587 | Inorg. Chem. 2012, 51, 7551−7560

Table 4. Calculated Molecular Orbitals for $Ni[S_2PR_2]_2$ Containing Ni 3d Character[a]

$Ni[S_2PR_2]_2$	MO	d orbital	% Ni 3d	% S 3p	energy (eV)
R = *o*-$CF_3C_6H_4$ (**1**)	$2b_{1g}$	d_{xy}	47.0	39.2	−2.265
	$4b_{2g}$	d_{xz}	40.5	54.8	−5.848
	$3b_{3g}$	d_{yz}	46.2	41.6	−5.948
	$3a_g$	d_{z^2}	81.8	10.0	−6.154
	$2b_{3g}$	d_{yz}	13.6	6.8	−7.443
	$3b_{2g}$	d_{xz}	27.3	19.2	−7.494
	$2b_{2g}$	d_{xz}	19.5	22.8	−7.610
	$2a_g$	$d_{x^2-y^2}$	30.7	4.8	−7.655
	$1b_{1g}$	d_{xy}	37.1	54.1	−7.824
	$1b_{3g}$	d_{yz}	38.6	28.6	−7.857
	$1b_{2g}$	d_{xz}	5.5	15.4	−7.867
	$1a_g$	$d_{x^2-y^2}$	53.4	2.0	−7.950
R = *m*-$CF_3C_6H_4$ (**2**)	$2b_{1g}$	d_{xy}	48.4	38.8	−2.702
	$4b_{2g}$	d_{xz}	38.9	56.4	−6.171
	$3b_{3g}$	d_{yz}	42.8	44.8	−6.246
	$3a_g$	d_{z^2}	85.4	6.4	−6.502
	$3b_{2g}$	d_{xz}	38.2	18.4	−7.765
	$2b_{3g}$	d_{yz}	5.5	3.0	−7.781
	$2b_{2g}$	d_{xz}	16.4	18.0	−7.897
	$2a_g$	$d_{x^2-y^2}$	32.2	4.8	−7.989
	$1b_{3g}$	d_{yz}	44.3	27.6	−8.082
	$1b_{1g}$	d_{xy}	36.6	56.4	−8.159
	$1b_{2g}$	d_{xz}	5.2	14.4	−8.195
	$1a_g$	$d_{x^2-y^2}$	52.8	2.0	−8.272
R = *p*-$CF_3C_6H_4$ (**3**)	$2b_{1g}$	d_{xy}	47.5	38.0	−2.822
	$4b_{2g}$	d_{xz}	38.9	56.8	−6.282
	$3b_{3g}$	d_{yz}	42.9	44.8	−6.359
	$3a_g$	d_{z^2}	88.3	3.6	−6.617
	$3b_{2g}$	d_{xz}	28.0	12.3	−7.855
	$2b_{3g}$	d_{yz}	10.5	7.2	−7.870
	$2b_{2g}$	d_{xz}	24.9	26.4	−7.979
	$2a_g$	$d_{x^2-y^2}$	30.7	5.6	−8.082
	$1b_{3g}$	d_{yz}	44.3	27.6	−8.193
	$1b_{1g}$	d_{xy}	36.6	56.6	−8.267
	$1b_{2g}$	d_{xz}	6.4	15.4	−8.280
	$1a_g$	$d_{x^2-y^2}$	56.1	2.0	−8.370
R = C_6H_5 (**4**)	$2b_{1g}$	d_{xy}	48.5	39.2	−2.205
	$4b_{2g}$	d_{xz}	38.7	56.8	−5.680
	$2b_{3g}$	d_{yz}	42.6	45.2	−5.755
	$3a_g$	d_{z^2}	88.2	3.6	−6.019
	$2b_{3g}$	d_{yz}	6.3	5.6	−7.161
	$3b_{2g}$	d_{xz}	16.3	6.0	−7.177
	$2b_{2g}$	d_{xz}	29.6	31.6	−7.347
	$2a_g$	$d_{x^2-y^2}$	16.3	6.0	−7.387
	$1b_{3g}$	d_{yz}	48.5	28.6	−7.575
	$1b_{2g}$	d_{xz}	13.3	22.0	−7.585
	$1b_{1g}$	d_{xy}	36.4	56.8	−7.667
	$1a_g$	$d_{x^2-y^2}$	70.3	2.0	−7.729
R = CH_3 (**5**)	$2b_{1g}$	d_{xy}	51.4	42.0	−2.354
	$2b_{2g}$	d_{xz}	40.4	57.6	−5.887
	$2b_{3g}$	d_{yz}	41.5	47.2	−5.905
	$2a_g$	d_{z^2}	88.5	3.6	−6.195
	$1b_{2g}$	d_{xz}	59.7	39.2	−7.537
	$1b_{3g}$	d_{yz}	58.1	28.8	−7.680
	$1a_g$	$d_{x^2-y^2}$	87.3	3.6	−7.828
	$1b_{1g}$	d_{xy}	35.9	57.6	−7.837

[a]The MO symmetry labels correspond to those used in Figure 6.

Time-Dependent Density Functional Theory Calculations. To aid in our interpretation of the UV−vis spectra shown in Figure 4 and support our tentative conclusions that the increased HOMO−LUMO for $Ni[S_2P(o\text{-}CF_3C_6H_4)_2]_2$ (**1**) vs $Ni[S_2P(m\text{-}CF_3C_6H_4)_2]_2$ (**2**), $Ni[S_2P(p\text{-}CF_3C_6H_4)_2]_2$ (**3**), and $Ni[S_2PPh_2]_2$ (**4**) is responsible for the observed differences, time-dependent density functional theory (TDDFT) calculations were performed. Overall, the simulated TDDFT spectra of **1**−**4** are in excellent agreement with the experimental data. At high energy (between 31 000 and 32 000 cm^{-1}), the calculations show ligand-to-metal charge transfer (LMCT) transitions, the largest of which involves an occupied ligand-based orbital of b_{3u} symmetry and the LUMO (b_{1g}; Figure 7).

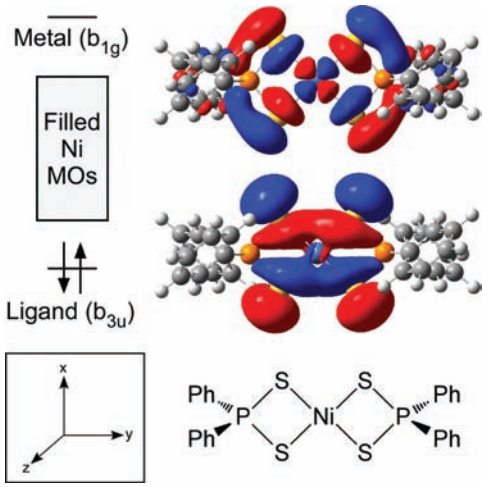

Figure 7. Natural transition orbitals of the ligand and metal-based molecular orbitals participating in the most intense LMCT transition at 31 314 cm^{-1} in the TDDFT spectrum of $Ni[S_2PPh_2]_2$ (**4**).

At lower energy, the calculations show a single weak LMCT transition near 25 000 cm^{-1}. The calculations show the first d−d transition, which corresponds to $2a_g \rightarrow$ LUMO ($2b_{1g}$), around 18 000 cm^{-1} and three closely matched d−d transitions that involve excitations from the $3a_g$, $4b_{2g}$, and $3b_{3g}$ orbitals to the LUMO ($2b_{1g}$) near 11 000 cm^{-1}. The relatively good agreement between the calculated transition energies with the peak positions observed experimentally provide confidence in our interpretation of the UV−vis data, which can be summarized for **1**−**4** as having a strong LMCT band at 30 000 cm^{-1} with a weak LMCT shoulder at 25 000 cm^{-1} and lower energy peaks associated with d−d transitions between the ^1A_g ground state and the $^1B_{1g}$, $^1B_{3g}$, and $^1B_{2g}$ excited states. We refrain from comparing the relative intensities of the experimental peaks with the calculated oscillator strengths for the d−d transitions because spin−orbit coupling, which gives these features intensity in the UV−vis spectra, was not included in the DFT calculations. As a result, there is no appreciable oscillator strength associated with the calculated d−d transitions (Table 5).

To graphically compare the position and splitting of the calculated low energy features in the spectra for **1**−**4**, the calculated oscillator strengths in Figure 8 have been artificially increased for the d−d transitions. For **2**−**4**, both experiment and theory show that the energies for the d−d transitions are nearly identical (Table 5), which is exemplified using the dotted lines in Figure 8. However, for $Ni[S_2P(o\text{-}CF_3C_6H_4)_2]_2$ (**1**), the TDDFT and experimental UV−vis data show a high energy

dx.doi.org/10.1021/ic3001587 | Inorg. Chem. 2012, 51, 7551−7560

Table 5. TD-DFT Calculated Transitions and Transition Assignments for $Ni[S_2PR_2]_2$ Complexes

	R = o-$CF_3C_6H_4$		R = m-$CF_3C_6H_4$		R = p-$CF_3C_6H_4$		R = C_6H_5	
transition (primary)	energy (cm^{-1})	oscillator strength	energy (cm^{-1})	oscillator strength	energy (cm^{-1})	oscillator strength	energy (cm^{-1})	oscillator strength
$3a_g \rightarrow 2b_{1g}$	11179	0.000	10192	0.000	10244	0.000	10329	0.000
$4b_{2g} \rightarrow 2b_{1g}$	11302	0.000	10388	0.000	10417	0.000	10476	0.000
$3b_{3g} \rightarrow 2b_{1g}$	11685	0.000	10767	0.000	10795	0.000	10845	0.000
$2a_g \rightarrow 2b_{1g}$	18396	0.000	17447	0.000	17475	0.000	17513	0.000
LMCT	24344	0.005	23068	0.005	23051	0.006	23121	0.005
LMCT (major)	31754	0.666	31463	0.734	31313	0.763	31314	0.977

shift of approximately 850−1000 cm^{-1} for all four d−d transitions, as well as the low energy LMCT peak near 25 000 cm^{-1}. Overall, this is consistent with the ground state DFT calculations and can be attributed to the increased HOMO−LUMO gap of **1** relative to **2**−**4**.

Comparison of Reported UV−Vis Assignments for $Ni[S_2PR_2]_2$. The electronic structure and UV−vis spectra for Ni(II) dithiophosphinates have been previously evaluated in several studies, and there exist conflicting reports regarding the relative ordering of molecular orbitals for $Ni[S_2PR_2]_2$ and the corresponding UV−vis assignments.[43,44] While it is generally acknowledged that the LUMO contains Ni d_{xy} character, the ordering of the subsequent Ni-based molecular orbitals has been disputed, particularly with regards to the identity of the HOMO (a_g vs b_{2g} or b_{3g}). Our ground state DFT data are most consistent with previously reported conclusions based on magnetic circular dichroism[44] and suggest that the HOMO is best described as an orbital of b_{2g} symmetry in the D_{2h} point group. However, the TDDFT calculations reveal that the low-energy d−d feature in the UV−vis spectra for the $Ni[S_2PR_2]_2$ complexes consists of nearly overlapping transitions from orbitals of a_g, b_{2g} (HOMO), and b_{3g} symmetry. The close energy of these transitions, which manifest as only one feature in the UV−vis spectra, may account for some of the inconsistencies in spectral interpretation and molecular orbital assignments.

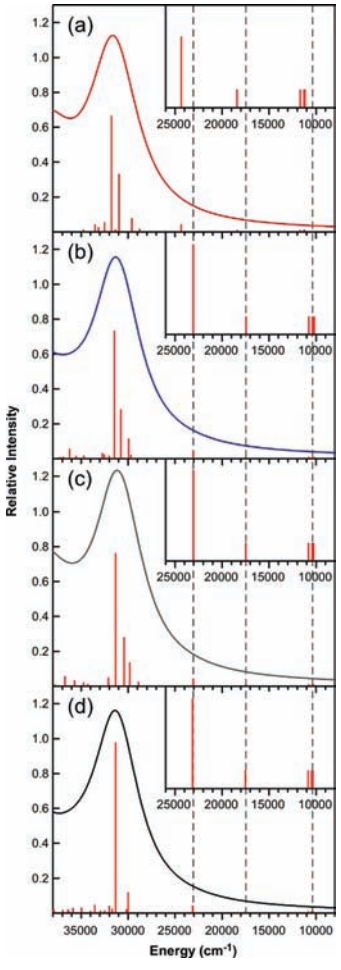

Figure 8. TD-DFT simulated spectra (solid lines) and calculated transitions (bars) for $Ni[S_2PR_2]_2$ complexes: (a) $Ni[S_2P(o\text{-}CF_3C_6H_4)_2]_2$ (**1**, red), (b) $Ni[S_2P(m\text{-}CF_3C_6H_4)_2]_2$ (**2**, blue), (c) $Ni[S_2P(p\text{-}CF_3C_6H_4)_2]_2$ (**3**, gray), and (d) $Ni[S_2PPh_2]_2$ (**4**, black). The insets show the magnified TD-DFT transitions between 8000 and 26 000 cm^{-1}. The oscillator strengths of these transitions, which are provided in Table 5, have been artificially increased to compare their relative positions.

CONCLUDING REMARKS

In summary, we report here that $HS_2P(o\text{-}CF_3C_6H_4)_2$ reacts differently than HS_2PR_2 (R = m-$CF_3C_6H_4$, p-$CF_3C_6H_4$, and Ph) with $NiCl_2$. Although the molecular geometry for the resulting $Ni[S_2P(o\text{-}CF_3C_6H_4)_2]_2$ (**1**) varies only slightly in comparison to **2**−**4**, the electronic structure of **1** is unusually distinct and shows a substantially increased gap between the LUMO and the occupied molecular orbitals. The origin of the increased destabilization of the LUMO in **1** compared to **2**−**4** can be reasonably interpreted as arising from increased covalent mixing in the Ni−S σ bonds formed between the Ni $3d_{xy}$ orbitals and the S 3p lone pairs.[55] The unique electronic structure of $Ni[S_2P(o\text{-}CF_3C_6H_4)_2]_2$ is noteworthy because $HS_2P(o\text{-}CF_3C_6H_4)_2$ exhibits exceptionally high selectivity for minor actinides compared to other diaryldithiophosphinates.[39]

While it is obvious that the chemistries of nickel and actinides are vastly different and that transition metals do not represent surrogates to understand electronic structure and bonding in f elements, the square planar $Ni[S_2PR_2]_2$ complexes do provide a highly symmetric and well-established coordination environment that is sensitive to subtle differences in the ligand electronic structure. By holding the metal identity constant, metal contributions to bonding remain equivalent, and electronic variations associated with the extracting ligand can be directly probed. Here, the UV−vis and TDDFT analysis identified that the HOMO−LUMO energy gap was directly related to the extractant identity and correlated with the ligand performance in minor actinide separations chemistry. Given that d^8 square-planar complexes represent a class of compounds that have been heavily studied, it seems likely that other spectroscopic techniques previously employed to characterize Ni^{2+} ligand field effects could also be used to identify special electronic properties associated with $S_2P(o\text{-}CF_3C_6H_4)_2^-$ vs

dx.doi.org/10.1021/ic3001587 | Inorg. Chem. 2012, 51, 7551−7560

$S_2P(m\text{-}CF_3C_6H_4)_2^-$, $S_2P(p\text{-}CF_3C_6H_4)_2^-$, and $S_2PPh_2^-$ anions. Hence, we are currently in the process of investigating the origin of the unique electronic structure of $Ni[S_2P(o\text{-}CF_3C_6H_4)_2]_2$ using S K-edge X-ray absorption spectroscopy and TDDFT calculations in support of efforts to advance extractant design relevant to minor actinide separations.

EXPERIMENTAL SECTION

The bis(trifluoromethylphenyl)dithiophosphinic acids $HS_2P(o\text{-}CF_3C_6H_4)_2$, $HS_2P(m\text{-}CF_3C_6H_4)_2$, and $HS_2P(p\text{-}CF_3C_6H_4)_2$ were prepared as previously described.[37,39] $Ni[S_2PPh_2]$ (**4**) was prepared as previously described using HS_2PPh_2 (Alfa Aesar).[45] $NiCl_2$ and $NiCl_2{\cdot}6H_2O$ (Strem) were used as received. H_2O was purified to 18.2 MW-cm resistivity using a Thermo-Scientific Barnstead Nanopure water purification system. All reactions were carried out in the air with solvents that were used as received from commercial sources. $CDCl_3$ (Aldrich) was used as received. Elemental analyses were carried out by Midwest MicroLab, LLC (Indianapolis, IN). The infrared spectra were recorded on a Nicolet Magna-IR System 750 spectrometer as KBr pellets. The ^1H, ^{31}P, and ^{19}F NMR data were obtained using a Bruker Avance NMR spectrometer at 300.1 MHz, 121.5 MHz, and 282.4 MHz, respectively. Chemical shifts are reported in δ units (positive shifts to high frequency) relative to TMS (^1H), H_3PO_4 (^{31}P), or $CFCl_3$ (^{19}F). The UV−vis spectra were collected on a Varian Cary 6000i UV−vis−NIR Spectrophotometer. Molar absorptivity (ε) values were determined by plotting measured absorbance values at three $Ni[S_2PR_2]_2$ concentrations ranging between 10^{-4} and 10^{-5} M.

Bis[bis(*o*-trifluoromethylphenyl)dithiophosphinato]Ni(II), $Ni[S_2P(o\text{-}CF_3C_6H_4)_2]_2$ (1). A solution of $HS_2P(o\text{-}CF_3C_6H_4)_2$ (0.401 g, 1.03 mmol) in EtOH (15 mL) was added to a solution of $NiCl_2$ (0.0673 g, 0.519 mmol) in H_2O (15 mL). A magenta precipitate immediately formed. The mixture was stirred for 3 h at room temperature. The mixture was filtered, and the solid was washed with H_2O (3 × 10 mL) and EtOH (3 × 5 mL) and allowed to evaporate to dryness in air. The solid was dissolved in a 1:8 hexane/CH_2Cl_2 solution, filtered, and crystallized by slow evaporation to yield a crystalline magenta solid. Yield: 0.290 g (70%). The solid could also be crystallized by cooling concentrated CH_2Cl_2 or acetone solutions. Anal. Calcd. for $C_{28}H_{16}F_{12}NiP_2S_2$: C, 40.6; H, 1.94; P, 7.47; F, 27.5. Found: C, 40.6; H, 1.99; P, 7.69; F, 27.2. ^1H NMR ($CDCl_3$, 20 °C): δ 7.64−7.74 (m, *meta*,*para*-H, 8H), 7.89 (t, $^3J_{HH}$ = 7 Hz, *meta*-H, 4H), 8.95 (dd, $^3J_{PH}$ = 19 Hz, $^3J_{HH}$ = 8 Hz, ortho-H, 4H). $^{31}P\{^1H\}$ NMR ($CDCl_3$, 20 °C): δ 92.3. $^{19}F\{^1H\}$ NMR ($CDCl_3$, 20 °C): δ −57.6 (s, CF_3). IR (cm^{-1}): 481 w, 504 w, 574 s, 589 m, 594 w, 622 m, 646 m, 669 w, 709 m, 737 w, 772 s, 783 m, 887 w, 967 w, 996 w, 1036 s, 1097 s, 1115 s, 1121 s, 1139 s, 1151 sh, 1172 sh, 1182 s, 1263 s, 1291 m, 1309 vs, 1437 m, 1473 w, 1571 w, 1591 w, 3027 w, 3070 m. UV−vis (CH_2Cl_2): 30 200 cm^- (ε = 26 900 M^{-1} cm^{-1}), 25 500 cm^- (ε = 2120 M^{-1} cm^{-1}), 18 800 cm^- (ε = 143 M^{-1} cm^{-1}), 14 300 cm^- (ε = 111 M^{-1} cm^{-1}).

Bis[bis(*m*-trifluoromethylphenyl)dithiophosphinato]Ni(II), $Ni[S_2P(m\text{-}CF_3C_6H_4)_2]_2$ (2). H_2O (3 mL) was added to a mixture of $NiCl_2{\cdot}6H_2O$ (0.075 g, 0.32 mmol) and $HS_2P(m\text{-}CF_3C_6H_4)_2$ (0.242 g, 0.63 mmol) followed by CH_2Cl_2 (20 mL). The CH_2Cl_2 fraction slowly turned dark blue as the newly formed **2** dissolved in the organic layer. The mixture was stirred for 30 min at room temperature. The organic layer was separated and evaporated to dryness under a vacuum. The dark blue solid was dissolved in 10 mL of CH_2Cl_2, filtered, and stored at −20 °C to yield dark blue prisms. Yield: 0.093 g (35%). Anal. Calcd. for $C_{28}H_{16}F_{12}NiP_2S_2$: C, 40.6; H, 1.94; P, 7.47; F, 27.5. Found: C, 40.5; H, 1.95; P, 7.09; F, 27.2. ^1H NMR ($CDCl_3$, 20 °C): δ 7.66 (t, $^3J_{HH}$ = 8 Hz, *meta*-H, 4H), 7.86 (d, $^3J_{HH}$ = 7 Hz, *para*-H, 4H), 7.90 (dd, $^3J_{PH}$ = 14 Hz, $^3J_{HH}$ = 8 Hz, *ortho*-H, 4H), 8.05 (d, $^3J_{PH}$ = 15 Hz, *ortho*-H, 4H). ^{31}P NMR ($CDCl_3$, 20 °C): δ 80.2 (p, $^3J_{PH}$ = 15 Hz). $^{19}F\{^1H\}$ NMR ($CDCl_3$, 20 °C): δ −64.1 (s, CF_3). IR (cm^{-1}): 467 w, 507 w, 535 w, 577 s, 583 sh, 614 w, 629 m, 639 s, 653 m, 656 m, 677 w, 695 s, 718 s, 742 w, 800 s, 813 s, 899 m, 915 m, 934 w, 943 w, 996 m, 1075 s, 1092 sh, 1112 vs, 1123 vs, 1145 s, 1165 s, 1174 sh, 1275 s, 1312 s, 1328 vs, 1418 s, 1429 m, 1478 w, 1602 m, 3045 sh, 3068 m. UV−vis (CH_2Cl_2): 29 800 cm^- (ε = 23300 M^{-1} cm^{-1}), 24 600 cm^- (ε = 1590 M^{-1} cm^{-1}), 17 700 cm^- (ε = 96 M^{-1} cm^{-1}), 13 500 cm^- (ε = 89 M^{-1} cm^{-1}).

Bis[bis(*p*-trifluoromethylphenyl)dithiophosphinato]Ni(II), $Ni[S_2P(p\text{-}CF_3C_6H_4)_2]_2$ (3). H_2O (3 mL) was added to a mixture of $NiCl_2{\cdot}6H_2O$ (0.035 g, 0.15 mmol) and $HS_2P(p\text{-}CF_3C_6H_4)_2$ (0.114 g, 0.295 mmol) followed by CH_2Cl_2 (15 mL). The CH_2Cl_2 layer slowly turned dark blue as the newly formed **3** dissolved in the organic layer. The mixture was stirred for 30 min at room temperature. The organic layer was separated and evaporated to dryness under a vacuum. The dark blue solid was dissolved in 12 mL of CH_2Cl_2, filtered, and stored at −20 °C to yield 57 mg of dark blue prisms. The mother liquor was concentrated to 4 mL and stored at −20 °C to yield an additional 21 mg of dark blue prisms. Yield: 0.078 g (64%). Anal. Calcd. for $C_{28}H_{16}F_{12}NiP_2S_2$: C, 40.6; H, 1.94; F, 27.5. Found: C, 40.6; H, 1.98; F, 27.5. ^1H NMR ($CDCl_3$, 20 °C): δ 7.78 (d, $^3J_{HH}$ = 7 Hz, *meta*-H, 8H), 7.89 (dd, $^3J_{PH}$ = 13 Hz, $^3J_{HH}$ = 8 Hz, *ortho*-H, 8H). $^{31}P\{^1H\}$ NMR ($CDCl_3$, 20 °C): δ 79.6. $^{19}F\{^1H\}$ NMR ($CDCl_3$, 20 °C): δ −64.6 (s, CF_3). IR (cm^{-1}): 498 w, 525 w, 593 sh, 602 s, 620 m, 633 w, 643 m, 708 s, 735 w, 783 w, 835 s, 960 w, 974 w, 1016 s, 1062 vs, 1107 s, 1127 s, 1142 s, 1176 s, 1287 w, 1323 vs, 1396 s, 1500 w, 1571 w, 1609 m, 1811 w, 1931 m, 3047 w, 3092 w. UV−vis (CH_2Cl_2): 29 800 cm^- (ε = 34 100 M^{-1} cm^{-1}), 24 600 cm^- (ε = 2650 M^{-1} cm^{-1}), 17 700 cm^- (ε = 149 M^{-1} cm^{-1}), 13 500 cm^- (ε = 140 M^{-1} cm^{-1}).

Crystallographic Details. Single crystals of **1**−**3** obtained from CH_2Cl_2 were mounted in a nylon cryoloop with Paratone-N oil under an argon gas flow. Single crystals of **4** were prepared as previously described.[45] The data were collected on a Bruker D8 diffractometer, with an APEX II charge-coupled-device (CCD) detector, and cooled to 120(1) K using an American Cryoindustries low temperature device. The instrument was equipped with graphite monochromatized Mo Kα X-ray source (λ = 0.71073 Å) and a 0.5 mm monocapillary. A hemisphere of data was collected using ω scans, with 10−30 s frame exposures and 0.5° frame widths. Data collection and initial indexing and cell refinement were handled using APEX II software.[56] Frame integration, including Lorentz-polarization corrections, and final cell parameter calculations were carried out using SAINT+ software.[57] The data were corrected for absorption using redundant reflections and the SADABS program.[58] Decay of reflection intensity was not observed as monitored *via* analysis of redundant frames. The structure was solved using direct methods and difference Fourier techniques. All hydrogen atom positions were idealized. The final refinement included anisotropic temperature factors on all non-hydrogen atoms. Structure solution, refinement, graphics, and creation of publication materials were performed using SHELXTL.[59] Data collection and refinement details are listed in Table 1.

Theoretical Calculations. UV−vis spectra were calculated at geometries optimized with density functional theory (DFT) in the gas phase with the hybrid functional B3LYP[60,61] as implemented in Gaussian 09.[25] Ni was modeled with the effective core potential and associated basis sets of Hay and Wadt (LANL2DZ)[62] augmented with a set of f polarization functions (exponent = 3.130).[63] All other atoms were modeled using a Pople style double-ζ 6-31G(d′,p′) all-electron basis set with polarization functions optimized for heavy atoms.[64,65] From these geometries, the spectra were simulated using time dependent density functional theory (TDDFT). Specifically, this analysis involves a linear response calculation for extracting the probability amplitudes from the transition densities and dipole moments between the calculated excited states and the ground state.[66] Natural transition orbital analysis was performed to further validate the individual TDDFT excitiations.[67]

ASSOCIATED CONTENT

Supporting Information

X-ray crystallographic data (CIF format). Atomic coordinates, Mullikan charges, and bond distances and angles for calculated structures of **1**−**5**. This material is available free of charge *via* the Internet at http://pubs.acs.org.

dx.doi.org/10.1021/ic3001587 | *Inorg. Chem.* 2012, 51, 7551−7560

AUTHOR INFORMATION

Corresponding Author

*E-mail: stosh@lanl.gov (S.A.K.); LAUR 12-00235.

Notes

The authors declare no competing financial interest.

ACKNOWLEDGMENTS

We would like to thank Drs. Dean R. Peterman and John L. Klaehn for initially providing a sample of $HS_2P(o\text{-}CF_3C_6H_4)_2$. This work was supported by U.S. Department of Energy, Office of Basic Energy Sciences, Division of Chemical Sciences, Geosciences, and Biosciences (Heavy Element Chemistry Program); the U.S. Department of Energy, Office of Nuclear Energy (Fuel Cycle R&D Program); the Glenn T. Seaborg Institute Postdoctoral Fellowship (S.R.D.); and a LANL Director's Postdoctoral Fellowship (J.M.K.). Los Alamos National Laboratory is operated by Los Alamos National Security, LLC, for the National Nuclear Security Administration of U.S. Department of Energy under Contract DEAC52-06NA25396.

REFERENCES

(1) Salvatores, M. *Nucl. Eng. Des.* **2005**, *235*, 805−816.
(2) Ogawa, T.; Minato, K.; Okamoto, Y.; Nishihara, K. *J. Nucl. Mater.* **2007**, *360*, 12−15.
(3) Ewing, R. C. *MRS Bull.* **2008**, *33*, 338−340.
(4) Lenzen, M. *Energy Convers. Manage.* **2008**, *49*, 2178−2199.
(5) Salvatores, M.; Palmiotti, G. *Prog. Part. Nucl. Phys.* **2011**, *66*, 144−166.
(6) Nash, K. L. *Solvent Extr. Ion Exch.* **1993**, *11*, 729−768.
(7) Nilsson, M.; Nash, K. L. *Solvent Extr. Ion Exch.* **2007**, *25*, 665−701.
(8) Braley, J. C.; Grimes, T. S.; Nash, K. L. *Ind. Eng. Chem. Res.* **2012**, *51*, 627−636.
(9) Choppin, G. R. *J. Less-Common Met.* **1983**, *93*, 323−330.
(10) Choppin, G. R.; Silva, R. J. *J. Inorg. Nucl. Chem.* **1956**, *3*, 153−154.
(11) Smith, H. L.; Hoffman, D. C. *J. Inorg. Nucl. Chem.* **1956**, *3*, 243−247.
(12) Surls, J. P., Jr.; Choppin, G. R. *J. Inorg. Nucl. Chem.* **1957**, *4*, 62−73.
(13) Chiarizia, R.; Danesi, P. R.; Scibona, G.; Magon, L. *J. Inorg. Nucl. Chem.* **1973**, *35*, 3595−3604.
(14) Svantesson, I.; Hangstroem, I.; Persson, G.; Liljenzin, J. O. *Radiochem. Radioanal. Lett.* **1979**, *37*, 215−222.
(15) Danesi, P. R.; Chiarizia, R.; Rickert, P.; Horwitz, E. P. *Solvent Extr. Ion Exch.* **1985**, *3*, 111−147.
(16) Brigham, D.; Badajoz, C.; Cote, G.; Nash, K. L. *Solvent Extr. Ion Exch.* **2011**, *29*, 270−291.
(17) Zhu, Y.; Chen, J.; Choppin, G. R. *Solvent Extr. Ion Exch.* **1996**, *14*, 543−553.
(18) Zhu, Y.; Chen, J.; Jiao, R. *Solvent Extr. Ion Exch.* **1996**, *14*, 61−68.
(19) Hill, C.; Madic, C.; Baron, P.; Ozawa, M.; Tanaka, Y. *J. Alloys Compd.* **1998**, *271*−*273*, 159−162.
(20) Modolo, G.; Odoj, R. *J. Alloys Compd.* **1998**, *271*−*273*, 248−251.
(21) Bhattacharyya, A.; Mohapatra, P. K.; Manchanda, V. K. *Solvent Extr. Ion Exch.* **2007**, *25*, 27−39.
(22) Dam, H. H.; Reinhoudt, D. N.; Verboom, W. *Chem. Soc. Rev.* **2007**, *36*, 367−377.
(23) Kolarik, Z. *Chem. Rev.* **2008**, *108*, 4208−4252.
(24) Xu, Q.; Wu, J.; Chang, Y.; Zhang, L.; Yang, Y. *Radiochim. Acta* **2008**, *96*, 771−779.
(25) Lumetta, G. J.; Gelis, A. V.; Vandegrift, G. F. *Solvent Extr. Ion Exch.* **2010**, *28*, 287−312.
(26) Modolo, G.; Kluxen, P.; Geist, A. *Radiochim. Acta* **2010**, *98*, 193−201.
(27) Lewis, F. W.; Harwood, L. M.; Hudson, M. J.; Drew, M. G. B.; Desreux, J. F.; Vidick, G.; Bouslimani, N.; Modolo, G.; Wilden, A.; Sypula, M.; Vu, T.-H.; Simonin, J.-P. *J. Am. Chem. Soc.* **2011**, *133*, 13093−13102.
(28) Ozcubukcu, S.; Mandal, K.; Wegner, S.; Jensen, M. P.; He, C. *Inorg. Chem.* **2011**, *50*, 7937−7939.
(29) Bremer, A.; Ruff, C. M.; Girnt, D.; Muellich, U.; Rothe, J.; Roesky, P. W.; Panak, P. J.; Karpov, A.; Mueller, T. J. J.; Denecke, M. A.; Geist, A. *Inorg. Chem.* **2012**, *51*, 5199−5207.
(30) Diamond, R. M.; Street, K., Jr.; Seaborg, G. T. *J. Am. Chem. Soc.* **1954**, *76*, 1461−1469.
(31) Jensen, M. P.; Bond, A. H. *J. Am. Chem. Soc.* **2002**, *124*, 9870−9877.
(32) Kozimor, S. A.; Yang, P.; Batista, E. R.; Boland, K. S.; Burns, C. J.; Clark, D. L.; Conradson, S. D.; Martin, R. L.; Wilkerson, M. P.; Wolfsberg, L. E. *J. Am. Chem. Soc.* **2009**, *131*, 12125−12136.
(33) Minasian, S. G.; Keith, J. M.; Batista, E. R.; Boland, K. S.; Clark, D. L.; Conradson, S. D.; Kozimor, S. A.; Martin, R. L.; Schwarz, D. E.; Shuh, D. K.; Wagner, G. L.; Wilkerson, M. P.; Wolfsberg, L. E.; Yang, P. *J. Am. Chem. Soc.* **2012**, *134*, 5586−5597.
(34) Minasian, S. G.; Krinsky, J. L.; Rinehart, J. D.; Copping, R.; Tyliszczak, T.; Janousch, M.; Shuh, D. K.; Arnold, J. *J. Am. Chem. Soc.* **2009**, *131*, 13767−13783.
(35) Krinsky, J. L.; Minasian, S. G.; Arnold, J. *Inorg. Chem.* **2011**, *50*, 345−357.
(36) Keith, J. M.; Batista, E. R. *Inorg. Chem.* **2012**, *51*, 13−15.
(37) Daly, S. R.; Klaehn, J. R.; Boland, K. S.; Kozimor, S. A.; MacInnes, M. M.; Peterman, D. R.; Scott, B. L. *Dalton Trans.* **2012**, *41*, 2163−2175.
(38) Daly, S. R.; Keith, J. M.; Batista, E. R.; Boland, K. S.; Clark, D. L.; Kozimor, S. A.; Scott, B. L. *J. Am. Chem. Soc.* **2012**, accepted.
(39) Klaehn, J. R.; Peterman, D. R.; Harrup, M. K.; Tillotson, R. D.; Luther, T. A.; Law, J. D.; Daniels, L. M. *Inorg. Chim. Acta* **2008**, *361*, 2522−2532.
(40) Peterman, D. R.; Greenhalgh, M. R.; Tillotson, R. D.; Klaehn, J. R.; Harrup, M. K.; Luther, T. A.; Law, J. D. *Sep. Sci. Technol.* **2010**, *45*, 1711−1717.
(41) Jones, P. E.; Ansell, G. B.; Katz, L. *Chem. Commun.* **1968**, 78−79.
(42) Porta, P.; Sgamellotti, A.; Vinciguerra, N. *Inorg. Chem.* **1968**, *7*, 2625−2629.
(43) Tomlinson, A. A. G.; Furlani, C. *Inorg. Chim. Acta* **1969**, *3*, 487−494.
(44) Looney, Q.; Douglas, B. E. *Inorg. Chem.* **1970**, *9*, 1955−1957.
(45) Cavell, R. G.; Byers, W.; Day, E. D.; Watkins, P. M. *Inorg. Chem.* **1972**, *11*, 1598−1606.
(46) Joergensen, C. K. *J. Inorg. Nucl. Chem.* **1962**, *24*, 1571−1585.
(47) Livingstone, S. E.; Mihkelson, A. E. *Inorg. Chem.* **1970**, *9*, 2545−2551.
(48) Vorobyev, D. Y.; Plyusnin, V. F.; Ivanov, Y. V.; Grivin, V. P.; Larionov, S. V.; Lemmetyinen, H. *Chem. Phys.* **2003**, *289*, 359−369.
(49) Figgis, B. N.; Hitchman, M. A. *Ligand Field Theory and Its Applications*; Wiley-VCH: New York, 2000.
(50) Esterhuysen, C.; Kruger, G. J.; Blewett, G.; Raubenheimer, H. G. *Inorg. Chim. Acta* **2006**, *359*, 609−616.
(51) Benson, M. T.; Moser, M. L.; Peterman, D. R.; Dinescu, A. *THEOCHEM* **2008**, *867*, 71−77.
(52) Dinescu, A.; Benson, M. T. *J. Phys. Chem. A* **2008**, *112*, 12270−12280.
(53) Leavitt, C. M.; Gresham, G. L.; Benson, M. T.; Gaumet, J.-J.; Peterman, D. R.; Klaehn, J. R.; Moser, M.; Aubriet, F.; Van Stipdonk, M. J.; Groenewold, G. S. *Inorg. Chem.* **2008**, *47*, 3056−3064.
(54) Szilagyi, R. K.; Lim, B. S.; Glaser, T.; Holm, R. H.; Hedman, B.; Hodgson, K. O.; Solomon, E. I. *J. Am. Chem. Soc.* **2003**, *125*, 9158−9169.
(55) Albright, T. A.; Burdett, J. K.; Whangbo, M. *Orbital Interactions in Chemistry*; John Wiley & Sons: New York, 1985.

(56) *APEX II 1.08*; Bruker AXS, Inc.: Madison, WI.
(57) *SAINT+ 7.06*; Bruker AXS, Inc.: Madison, WI.
(58) Sheldrick, G. *SADABS 2.03*; University of Göttingen: Göttingen, Germany.
(59) *SHELXTL 6.14*; Bruker AXS, Inc.: Madison, WI.
(60) Lee, C.; Yang, W.; Parr, R. G. *Phys. Rev. B: Condens. Matter* **1988**, *37*, 785−789.
(61) Becke, A. D. *J. Chem. Phys.* **1993**, *98*, 5648−5652.
(62) Hay, P. J.; Wadt, W. R. *J. Chem. Phys.* **1985**, *82*, 299−310.
(63) Ehlers, A. W.; Boehme, M.; Dapprich, S.; Gobbi, A.; Hoellwarth, A.; Jonas, V.; Koehler, K. F.; Stegmann, R.; Veldkamp, A.; Frenking, G. *Chem. Phys. Lett.* **1993**, *208*, 111−114.
(64) Petersson, G. A.; Bennett, A.; Tensfeldt, T. G.; Al-Laham, M. A.; Shirley, W. A.; Mantzaris, J. *J. Chem. Phys.* **1988**, *89*, 2193−2218.
(65) Petersson, G. A.; Al-Laham, M. A. *J. Chem. Phys.* **1991**, *94*, 6081−6090.
(66) Elliott, P.; Furche, F.; Burke, K. Excited States from Time-Dependent Density Functional Theory. In *Reviews in Computational Chemistry*; Lipkowitz, K. B., Cundari, T. R., Eds.; Wiley: Hoboken, NJ, 2009; Vol. *26*, pp 91−165.
(67) Martin, R. L. *J. Chem. Phys.* **2003**, *118*, 4775−4777.